Scripta Materialia 149 (2018) 144–149

Contents lists available at ScienceDirect

Scripta Materialia

journal homepage: www.elsevier.com/locate/scriptamat

Regular article

Polycrystalline micropillars by a novel 3-D printing method and their behavior under compressive loads

M. Sadeq Saleh [a], Mehdi HamidVishkasougheh [b], Hussein Zbib [b,*], Rahul Panat [a,*]

[a] Department of Mechanical Engineering, Carnegie Mellon University, Pittsburgh, PA 15213, United States
[b] School of Mechanical and Materials Engineering, Washington State University, Pullman, WA 99164, United States

ARTICLE INFO

Article history:
Received 29 January 2018
Received in revised form 15 February 2018
Accepted 18 February 2018

Keywords:
Micropillar
3D printing
Nanoparticle printing
Size effect
Grain size
Mechanical properties
Compression
Buckling

ABSTRACT

We present an entirely new method of bottoms-up fabrication of polycrystalline micropillars using direct printing and sintering of nanoparticles in 3D and study their behavior under compression for different microstructures. The pillars showed brittle behavior with higher effective modulus for small grain sizes with high porosity, while highly ductile behavior with a lower effective modulus and larger grain sizes but low porosity. These unusual trends are explained by a porosity model. The results point to a novel method of fabricating micropillars with different microstructures to study fundamental materials science of polycrystalline materials at micro to meso-length scales.

Micropillar compression test is a popular method to study the mechanical behavior of various engineering materials for more than a decade [1–4]. Micropillars of different materials with a variety of sizes, textures, and microstructures [5] have been realized by using fabrication methods such as focused ion beam (FIB) milling [1,6,7], nano-imprinting [8], vapor deposition [9], and electrodeposition [10]. Each of the above methods has led to experiments that have contributed greatly to our knowledge of the behavior of materials at microscales. These methods, however, have their advantages as well as limitations in allowing the manufacture of samples of desired materials, geometries, and microstructures. For example, FIB milling can produce nano and microscale samples with precise dimensions from a wide variety of materials, but also results in ion implantation into the samples that may induce artificial size effects, or result in voids that affect their mechanical behavior [11]. In addition, for polycrystalline materials, obtaining different grain sizes (and hence the microstructures) for the same material is not straightforward. In case of electrochemical deposition and/or etching, the limitations are based on the chemical compatibility of the material being tested and difficulty in changing the microstructure [10]. For microscale samples, it was seen that the deformation mechanisms of elemental metals differ over three grain size ranges, namely, below 100 nm (nanocrystalline), between 100 nm and 1 μm (ultrafine grain), and above 1 μm (medium to large grains) [12,13]. For materials having ultrafine grains, the deformation was shown to be accommodated by grain boundary sliding and dislocation activity (unit or partial) sourced from the boundary [12,13]. The above work further suggests that creating new microstructures and geometries at microscales can help in the investigation of new scientific principles and the engineering of materials for specific applications.

Several developments in the manufacturing sciences have opened up the possibility of making devices and samples not possible in the past [14]. Bottoms-up manufacturing technique such as microscale 3D printing is among one such method, where nano or microparticles can be printed on 2D surfaces followed by sintering, that creates microscale geometries with a microstructure defined by the starting nano or microparticles [15–18]. We have recently developed a new manufacturing process where nanoparticles were arranged in 3D space at microscales in different shapes using pointwise printing in three dimensions followed by binder removal and nanoparticle sintering [16]. Complex 3D micro-lattice structures with truss members having diameters of 10s of microns with the microstructure defined by the nanoparticle size were fabricated using metal nanoparticles. During sintering of the nanoparticles, the porosity in the solid truss members can be controlled by the sintering temperature and time [16]. An example illustrated in Fig. S1 shows a silver micro lattice with near-fully dense truss members fabricated by this method. The truss members (Figs. S1b–c) can be considered as solid two-force elements, especially when their aspect ratio

* Corresponding authors.
E-mail addresses: zbib@wsu.edu (H. Zbib), rpanat@andrew.cmu.edu (R. Panat).

https://doi.org/10.1016/j.scriptamat.2018.02.027
1359-6462/

(length to the diameter) is high, as is Fig. S1b. The behavior of micropillars is thus a highly important engineering problem for microscale cellular/lattice materials.

The impetus for the present work is thus twofold. First, we wanted to fabricate polycrystalline micropillars using the recently discovered method of assembling metal nanoparticles in 3D space followed by sintering [16] and demonstrate its flexibility in creating samples with different microstructures and internal porosities. Second, we wanted to carry out a micropillar compression test on such samples with grain sizes ranging from hundreds of nanometers (fine grain microstructure) to a few microns (coarse grain microstructure) with different porosities and obtain their behavior under compression. The work thus advances fundamental materials science by using the latest developments in novel microscale manufacturing methods.

The micropillars fabrication by nanoparticle printing is shown in a schematic in Fig. 1(a), with details in section S1 of supporting information. Fig. 1(b, c) show square array of 25 pillars, and the pillar dimensions (90 μm outer diameter, 70 μm inner diameter, and about 600 μm in height) and the grain size distribution within a given pillar, respectively. We note that the pillar surface is "rough" and made up of silver grains formed from the sintered nanoparticles. Within the process optimization used for this study, the pillar axis could be maintained within about ±3°. We note that the hollow geometry was selected in this study to enable fabrication of taller pillars suitable for optical observation and strain recording under compression as described below. It is clear from Fig. 1 that the pillars can be directly printed to the final net shape in a single printing step followed by sintering. The time taken to print a single pillar is within a minute. Note that the grain size can be changed by either varying the starting nanoparticle size and/or the sintering conditions. Lastly, any material in nanoparticle form with particle size <500 nm can be printed, with the nanoparticles transforming into the grain, which can provide flexibility in choosing materials and microstructures.

The compressive mechanical behavior of micro-pillar arrays was investigated in a customized apparatus (Fig. S2) described in the supporting information, Section-S2. The SEM images of the grains and grain size distribution, and focused ion beam (FIB) sections of the pillars for different sintering conditions is shown in Fig. 2 and the statistics are given in Table 1. The grain sizes were measured by detecting boundaries in an SEM images by image processing software (Image J, NIH, Bethesda, MD) over at least three areas for each specimen. Gaussian normal curve was fitted on the area percentage distribution to calculate the mean grain size and bandwidth. At a lower sintering temperature of 250 °C, the mean grain size is of the order of about 250 nm, while at higher sintering temperatures of 350 °C and 450 °C, the mean grain size increased to about 2.9 μm, and 3.8 μm, respectively. For a sintering temperature of 550 °C, however, a near bimodal distribution with mean grain sizes at 3 μm and 7 μm (bimodality factor of 2.1) was observed as shown in Fig. 2(a). Since the pillars are made by sintering and growth of the nanoparticles, it is expected that the microstructure will have internal porosity. We carried out focused ion beam (FIB) section for a few cases to get an estimation of the porosity. The FIB section shown in Fig. 4 (b–d) show porosities at about 17–20% (pore size 250–300 nm), 15% (pore size ~1 μm), and <1% (pore size ~170 nm) for sintering

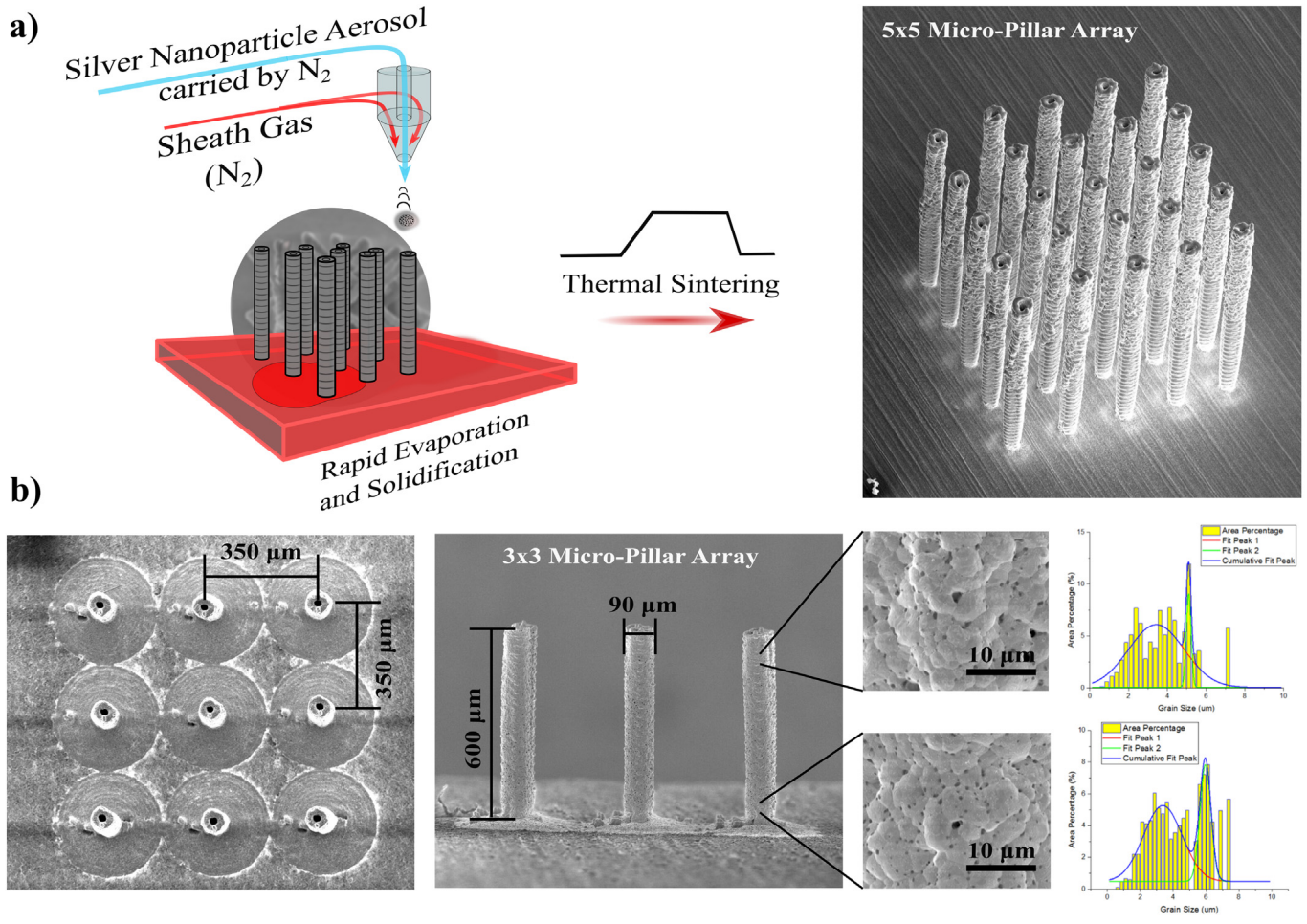

Fig. 1. (a) Schematic of the printing process showing the fabrication of the micro pillars. (b) A printed micropillar array in a 5 × 5 matrix. (c) A 3 × 3 micropillar array with pillar dimensions of 90 μm outer diameter, about 70 μm inner diameter, 350 μm spacing, and about 600 μm in height.

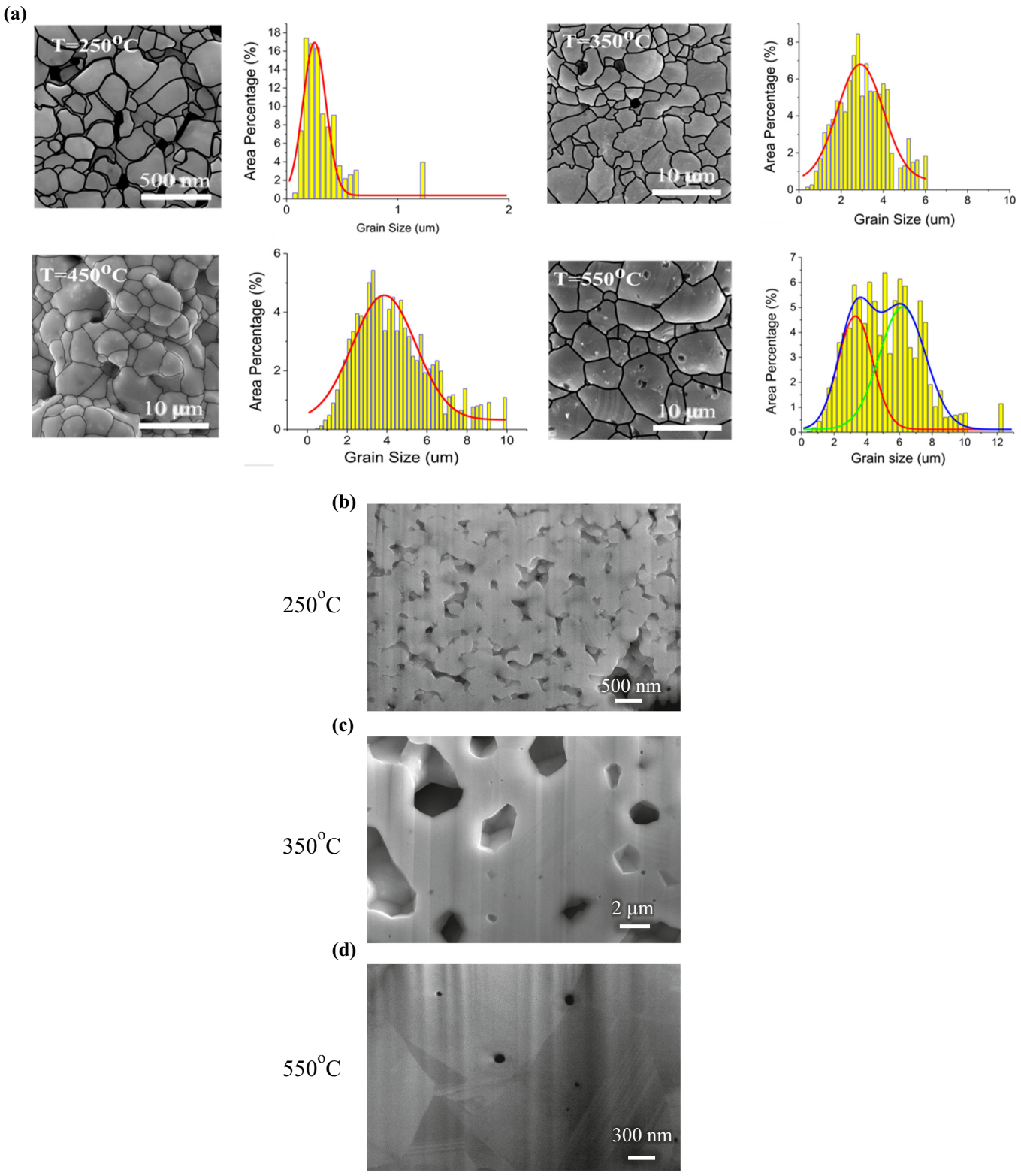

Fig. 2. (a) The microstructure and grain size distribution of the micropillars when sintered at four different holding temperatures. (b-d) Focused ion beam(FIB) section of the micropillar wall showing a porosities for the samples sintered at 250 °C, 350 °C, and 550 °C, respectively.

temperatures of 250 °C, 350 °C, and 550 °C, respectively. It is clear from the above that within some constraints, microscale pillars can be constructed by assembling nanoparticles followed by their sintering. Such an assembly was not possible in the past and gives rise to new avenues to obtain and study microstructures, shapes, etc.

Fig. 3(a) and (b) show the behavior of the micropillar arrays under compression for grain sizes shown in Fig. 2(a) with sintering temperatures of 250 °C and 550 °C. As the load increases, we see a linear region of response in both the cases at low loads. Prior to this linear portion, i.e. just when the loading starts, a non-linear portion of response is also

Table 1
Grain size measurement statistics and final sintering porosity.

Sintering temp		250 °C	350 °C	450 °C	550 °C
Grain size	Mean	249 ± 8 nm	2.91 ± 0.08 μm	3.86 ± 0.08 μm	3.31 ± 0.31 μm 6.18 ± 0.40 μm
	Bandwidth	±120 nm	±1.27 μm	±1.85 μm	±1.24 μm ±1.67 μm
Porosity					
Number of specimens		4	4	13	10
Total number of pillars		36	36	117	90

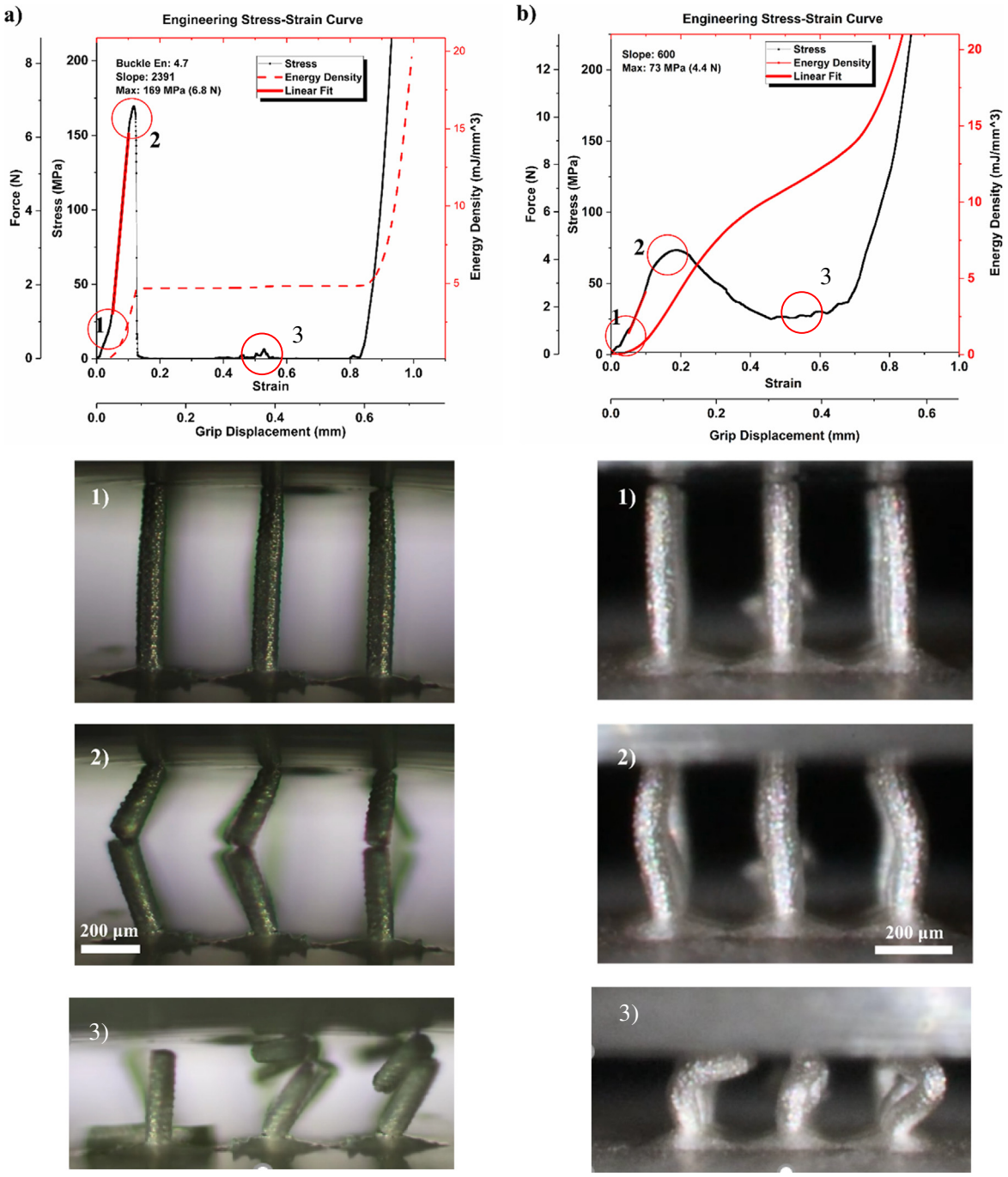

Fig. 3. Micropillars array stress-strain response in buckling compression test. A) Specimen buckled with ultrafine microstructure (250 nm) sintered at 250 °C holding temperature. The brittle fracture is captured in the bellow picture. B) Micropillars array showing more ductile behavior with higher strain energy absorbed before buckling. This specimen sintered at 550 °C resulted in bimodal grain microstructure with dual mean value of 3.3 mm and 6.1 mm.

observed and is attributed to the fact that the nine pillars within the array have a height variation of approximately ±3%. Beyond the linear portion of the curve, a high peak load of about 7 N was observed for the sample with small grain sizes vs a smaller peak load of about 4 N for the pillars having larger grain sizes. The peak load (or stress) was correlated with the time when the pillars show instability in the video recordings. This load, however, may differ from the classic buckling load for the pillars as the pillars have small eccentricity. Note that Fig. 3 also shows the images of the pillars at the start of the experiment, just after the peak stress, and when the load started to increase again (locations 1, 2, and 3, respectively). It is clear from Fig. 3(a) that the pillars with smallest grain sizes exhibit a brittle behavior with breakage of the pillars just when the instability occurs. The breakage appeared to happen without any plastic deformation. As the platen continued to be lowered, the pillars showed further cracking prior to complete disintegration. In contrast, Fig. 3(b) shows that in the case of large grain sizes, buckling happened at a lower stress compared to Fig. 3(a), but the pillars bend without breaking. In fact, as the platen continued to be lowered (location 3 in Fig. 3b), the pillar bent to a radius of about 50 μm, indicating a strain of >20% without breakage. The pillar behavior for the samples with 350 °C and 450 °C sintering was similar to that of Fig. 3(b). Fig. 4 shows the peak stress at buckling, the slope of the linear portion of the stress-strain plots, and the energy absorbed by the pillars prior to buckling (mJ/mm^3) plotted as a function of the grain size. It is clear that as the grain size increases, the peak load and the slope decreases, while the energy absorbed by the system prior to the instability also decreases. We observed that the energy is seen to increase with the introduction of bimodality for the largest grain size (i.e. for microstructure for pillars sintered at 550 °C in Fig. 2 and Table 1).

The compression behavior of the pillars shown in Figs. 3 and 4 gives rise to several interesting questions regarding the dependence of the instability of the pillars on their microstructure. For example, the classic Euler buckling model predicts that buckling load $P_{cr} = {}^{\pi^2 EI}/_{(KL)^2}$, where E is the elastic modulus of the material, I is the area moment of inertia, L is the column length, and K is the effective length factor that can be taken as 0.7 for the present case [19]. This clearly indicates that P_{cr} is dependent upon the modulus and sample geometry, and is expected to be independent of the grain size. From Figs. 3 and 4(a), however, the microstructure appears to affect the peak load. As stated before, the peak load may not represent buckling because of the geometric imperfections in the system and possibility of eccentricity. We also note that the above equation for P_{cr} is valid as long as no part of the column has yielded, which is a reasonable assumption in the linear portion of the graphs in Fig. 3.

To investigate this further, we considered the possibility of porosity affecting the elastic modulus, and in turn the P_{cr}. The slope of the stress-strain curves of the micropillars given in Fig. 4(b) clearly shows its dependence on the microstructure (i.e., grain size as well as porosity). Several studies in literature show a dependence of the elastic modulus on porosity, but do not consider grain size [20,21]. In these studies, the elastic modulus E for a given porosity $\varnothing$ is given by the empirical relation [22], $E(\varnothing) = E\,(1 - \varnothing/\varnothing_o)^n$, where, n is a power exponent that has been found to vary in measurements between 0.5 and 4, and $\varnothing_o$ is the critical porosity fraction ranging from 0.37 to 0.97 [21]. Unfortunately, we do not know the value of n for our system. In case of polycrystalline Cu samples, it was shown that the modulus reduces to about 5% of the bulk value for a porosity as low as 5% [20]. Silver nanoparticle films made by inkjet printing followed by thermal sintering showed an effective elastic modulus of about 5–7% of bulk silver when measured by the indentation technique [23]. We note that for the micropillars in the current study, the slope of the linear portion of the stress-strain curves in Fig. 3(a, b), can be considered as a ***lower bound*** of the effective

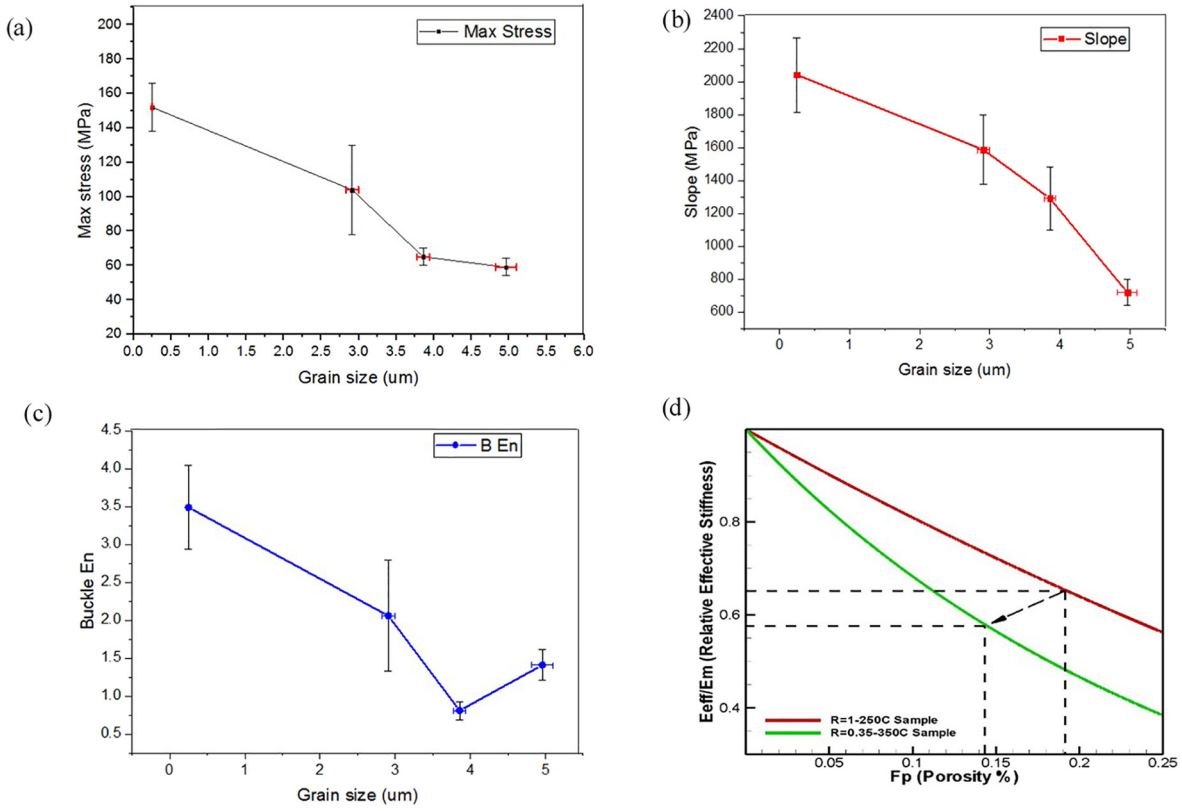

Fig. 4. (a) The maximum stress as a function of the grain size, (b) the slope of the linear portion of the pillar stress-strain plots as a function of the grain size, (c) the buckling energy (mJ/mm^3) as a function of the grain size, and (d) Relative elastic modulus vs porosity percentage based on two-phase model [23].

elastic modulus. This is because the pillars may have a small eccentricity inherent from the manufacturing process, lowering the measured effective elastic modulus. For the porosity in Fig. 2(b–d), the lower bound of the effective modulus, 2.3 GPa, which is about 3% of that for bulk silver, is thus within a reasonable range of that observed in literature [20,23].

This still leaves a question as to why we get decreasing peak stress with increasing sintering temperature (Fig. 4a) which is expected to reduce porosity (as confirmed by FIB sections in Fig. 2b, c, d). One of the possible reasons could be that the pillar imperfections may have resulted in localized yielding and some randomness in the buckling stress. However, the differences in the moduli shown in the data of Fig. 4(a) are statistically significant and the behavior under compressive load observed in Fig. 3(a, b) was repeated in every experiment. To further shed light on the dependence of buckling load on the combined effects of grain size and porosity, we decided to consider the combined effects of grain size and porosity on the modulus with the aim of capturing the data trends. We assume that the grains and pores are equiaxed and have a random distribution. The effective modulus by this model [24–26] is,

$$E_{eff} = f_c E_m \tag{1}$$

where, $f_c = (f_m)^2 R/(f_p + f_m R)$ and $R = D_p/D_g$, with f_c being continuous materials fraction volume, D_p being the pore size, D_g the material grain size, f_m being the material percentage, and f_p being the porosity percentage. Eq. (4) predicts nonlinear dependence of effective stiffness on porosity and strong dependence on pore size. In the present case, calculated R is about 1 and 0.35 for pillars sintered at 250 °C and 350 °C, respectively. We did not consider the case of the porosity for 550 °C as it is extremely low and the assumptions for the model of Eq. (1) (e.g. uniform pore distribution) are not valid. Fig. 4(d) shows the relative elastic modulus vs porosity percentage for given R ratios based on Eq. (1) [26]. It is clear from Fig. 4(d) that it is possible to have a reduction in stiffness with decreasing density of pores if each sample belongs to a different *R* value, a trend not captured by closed cell model [27] or the models discussed in [22]. The porosity model (Eq. 1) considered in the current study [24–26] thus shows the observed experimental trend, i.e. the effective stiffness can decrease with a decreasing porosity as indicated in the dashed arrow in the figure. We note that although the idealized model considered in Eq. (1) can predict the trend of effective stiffness reduction with decreasing porosity percentage, the predicted effective stiffness with this model is still more than measured values in the experiment. This implies that there are other parameters like spatial distribution of pores, pores shapes, geometry of pillars and imperfections that need to be characterized and their impacts on effective stiffness need to be clarified. From the above discussion, it can be inferred that measured effective stiffness is not only dependent on pore size, pore density and grain size but is also affected by large curvatures and geometric imperfections in certain regions of the pillar that can cause stress intensity. This, in turn, can lead to localized plastic deformation accompanied by dislocation pileups at grain boundaries in these regions while the rest of the pillar is still deforming elastically. Thus, such imperfections in line with porosity effects can be the main reason of difference among the measured effective stiffness and bulk stiffness of the pillars in this study and other sintered nanoparticle geometries observed in literature [20,23]. A more accurate treatment requires reducing such imperfections, and or full numerical elastic-plastic FE analyses, based on strain and or stress gradient plasticity theories [28], of a three-dimensional model which more accurately represent the geometry of the micropillars shown in Fig. 1. Nonetheless, the idealized analytical model presented in this paper provides reasonable explanation of the observed experimental trend. We anticipate the applications of the pillars and other 3D geometries shown in Fig. 1 and S1 in the areas of bioprobes, microscale heat sinks, flexible interconnects, catalysis, and energy storage solutions such as Li-ion batteries.

The results presented in this paper establish a versatile fabrication method for polycrystalline 3D micropillars where a wide range of microstructures can be realized with relatively simple changes to the fabrication process. Further, we could change the porosity and grain sizes within the pillars (from a few hundred nanometers to a few micrometers) by changes to the sintering conditions. The buckling behavior of the pillars was studied and shown to change from classic brittle to highly ductile with increasing grain size and reducing porosity. These trends are rationalized through a model that describes porosity effect on elasticity to predict the trends in effective elastic modulus. We thus obtain a rich set of geometries and microstructures of microscale 3D parts to gain an insight into structure-property relation of polycrystalline metals at a length scale of tens to hundreds of micrometers.

Acknowledgments

This work was supported by the National Science Foundation under Grant No. 1663511. We would like to thank Mr. Robert Lentz for his help during the experiments. The microscopy work was performed at the Nanoscience Fabrication and Characterization Facility at the University of Pittsburgh, under CMU-Pittsburgh collaborative agreement and the Franceschi Center at the Washington State University, Pullman WA.

Appendix A. Supplementary data

Supplementary data to this article can be found online at https://doi.org/10.1016/j.scriptamat.2018.02.027.

References

[1] J.R. Greer, W.C. Oliver, W.D. Nix, Acta Mater. 53 (6) (2005) 1821–1830.
[2] J.R. Greer, J.T.M. De Hosson, Prog. Mater. Sci. 56 (6) (2011) 654–724.
[3] R. Dou, B. Derby, Scr. Mater. 61 (5) (2009) 524–527.
[4] C.A. Volkert, E.T. Lilleodden, Philos. Mag. Lett. 86 (33–35) (2006) 5567–5579.
[5] M.A. Meyers, A. Mishra, D.J. Benson, Prog. Mater. Sci. 51 (4) (2006) 427–556.
[6] M.D. Uchic, D.M. Dimiduk, J.N. Florando, W.D. Nix, Science 305 (5686) (2004) 986.
[7] J.R. Greer, W.D. Nix, Phys. Rev. B 73 (24) (2006).
[8] S. Buzzi, M. Dietiker, K. Kunze, R. Spolenak, J.F. Löffler, Philos. Mag. Lett. 89 (10) (2009) 869–884.
[9] S. Lotfian, M. Rodríguez, K. Yazzie, N. Chawla, J. Llorca, J.M. Molina-Aldareguía, Acta Mater. 61 (12) (2013) 4439–4451.
[10] M. Mutoh, T. Nagoshi, T.-F.M. Chang, T. Sato, M. Sone, Microelectron. Eng. 111 (2013) 118–121.
[11] H. Bei, S. Shim, M. Miller, G. Pharr, E. George, Appl. Phys. Lett. 91 (11) (2007) 111915.
[12] H. Conrad, J. Narayan, Acta Mater. 50 (20) (2002) 5067–5078.
[13] H. Conrad, Mater. Sci. Eng. A 341 (1) (2003) 216–228.
[14] B.K. Paul, R. Panat, C. Mastrangelo, D. Kim, D. Johnson, J. Micro Nano-Manuf. 4 (4) (2016), 044001.
[15] X. Zheng, H. Lee, T.H. Weisgraber, M. Shusteff, J. DeOtte, E.B. Duoss, J.D. Kuntz, M.M. Biener, Q. Ge, J.A. Jackson, S.O. Kucheyev, N.X. Fang, C.M. Spadaccini, Science 344 (6190) (2014) 1373–1377.
[16] M.S. Saleh, C. Hu, R. Panat, Sci. Adv. 3 (3) (2017).
[17] D. Jang, L.R. Meza, F. Greer, J.R. Greer, Nat. Mater. 12 (10) (2013) 893–898.
[18] L.R. Meza, S. Das, J.R. Greer, Science 345 (6202) (2014) 1322–1326.
[19] R.G. Budynas, J.K. Nisbett, Shigley's Mechanical Engineering Design, McGraw-Hill, New York, 2008.
[20] E. Zhang, B. Wang, Int. J. Mech. Sci. 47 (4) (2005) 744–756.
[21] R.A. Hardin, C. Beckermann, Metall. Mater. Trans. A 38 (12) (2007) 2992–3006.
[22] C.W. Bert, J. Mater. Sci. 20 (6) (1985) 2220–2224.
[23] R. Dou, B. Xu, B. Derby, Scr. Mater. 63 (3) (2010) 308–311.
[24] Z. Fan, A. Miodownik, P. Tsakiropoulos, Mater. Sci. Technol. 9 (12) (1993) 1094–1100.
[25] P. Bartkowski, S. Spletzer, Porosity Effects on the Elastic Constants of Five Varieties of Silicon Carbide Ceramic, ARMY RESEARCH LAB ABERDEEN PROVING GROUND MD, 2001.
[26] A. Boccaccini, Z. Fan, Ceram. Int. 23 (3) (1997) 239–245.
[27] L.J. Gibson, M.F. Ashby, Cellular Solids: Structure and Properties, Cambridge University Press, 1999.
[28] H. Lyu, M. Hamid, A. Ruimi, H.M. Zbib, Int. J. Plast. 97 (2017) 46–63.